Section 3

Efficiency Physics and Model

The key physics to model the HETGS effective area comes in at the level of the single-grating diffraction efficiency $g_f(E, m)$ appearing in Equation 1.4. In order to achieve high diffraction efficiencies, we are operating outside the range of the simple diffraction theory[9] of opaque bars and instead in a region where the grating bars transmit and phase-shift the X-rays. Guided and assisted by Dale Graessle and his AXAF witness mirror work at NSLS[31], Tom Markert and Christie Nelson initiated grating synchrotron measurements of diffraction efficiency, reported in Nelson *et al.*[56] and Markert *et al.*[47]. These studies have allowed us to verify the phased non-rectangular model, provided reference standards for laboratory tests, and provided more accurate optical constant data for the materials in our gratings. The state of our synchrotron measurements and modelling efforts was most recently detailed by Flanagan *et al.*[25]. Although this work is ongoing, the fundamental result was a detailed physical model of grating diffraction that applies to individual gratings $g_f(E, m)$ and has been measured at many finely spaced energies. Cross-testing of several gratings in the X-GEF lab and at synchrotron facilities allows us to put constraints on the efficiency models produced from X-GEF tests.

3.1 Diffraction Theory and Models

3.1.1 Scalar Diffraction Theory

The model we use is the simple scalar (Kirchoff) diffraction theory [9]; rigorous diffraction theory, using the vector properties of the electromagnetic field and appropriate boundary conditions for the grating bars, is not required so long as the wavelength of the light being considered is much less than the period of the grating. Since we are dealing with, at most, wavelengths of 30 Å, and the grating period is no less than 2000 Å(for the HEG gratings) this condition is fulfilled fairly well. We note that the scalar model will begin to err at the lowest energies of interest, and that we will have to consider the more rigorous method (at least at the lower energies) as we continue to refine the model.

The general formula for the efficiency of a periodic grating, using the Kirchoff diffraction theory with the Fraunhofer approximation is ([9, 36]):

$$\eta_{(m)}(k) = 1/p^2 \times [\int_0^p e^{ik(\nu-1)z(\xi)-2\pi mi\xi/p} d\xi]^2 \tag{3.1}$$

where $\eta_{(m)}$ is the efficiency in the mth order, k is the wavenumber ($= 2\pi/\lambda$), ν ($= \nu(k)$) is the complex index of refraction, p is the grating period, and, $z(\xi)$ is the grating bar shape function. The bar shape function $z(\xi)$ may be thought of as the shape of the cross-section of the grating bar for X-rays normally incident on the grating surface.

In addition to the parameters indicated in equation 3.1, there are other factors which effect the measured diffraction efficiencies. These are the absorptions of the support film (see Figure 1.3) and the plating base. The grating is built up onto a thin (0.98 μm for the HEGs, 0.55 μm for the MEGs) polyimide film which provides mechanical support. In addition, there are very thin metallic films ($\simeq$ 200 Å of gold and 50 Å of chromium) which are used for the electroplating process. These films are essentially uniform over the grating and serve only to absorb (and not diffract) X-rays. However, their absorption introduces edge structure which has been investigated through testing at synchrotrons (described below).

Thus, the parameters for the scalar model (with absorption) of the HETG gratings are:

$\beta(k)$ and $\delta(k)$, the components of the index of refraction for gold

$z(\xi)$, the bar shape function (note that the grating period is not an explicit parameter, but only scales the bar shape)

t_{au}, the thickness of the gold plating base

t_{cr}, the thickness of the chromium plating base

t_{poly}, the thickness of the polyimide support film

$\beta_{polyimide}(k)$ and $\beta_{cr}(k)$, the imaginary parts of the index of refraction, which give the transmission of the support film and the plating base.

3.1.2 Rectangular Models

Consider the grating model without regard to the aborbing support layers. For a rectangular wire profile[68], i.e, where

$z(\xi) = h$ for $0 < \xi \leq p - a$, and

$z(\xi) = 0$ for $p - a < \xi \leq p$,

equation 3.1 becomes

$$\eta_{(m)}(k) = [\frac{sin(\frac{m\pi a}{p})}{m\pi}]^2 \times [1 + e^{-2k\beta h} - 2e^{-k\beta h} cos(k\delta h)] \qquad m \neq 0 \tag{3.2}$$

and

$$\eta_{(0)}(k) = (a/p)^2 + (1-a/p)^2 e^{-2k\beta h} + 2(a/p)(1-a/p)e^{-k\beta h}cos(k\delta h) \qquad m = 0. \tag{3.3}$$

Here a is the width of the space between grating lines and p is the period. As before, δ and β are the complex components of the index of refraction ν. Note that ν, δ, and β are all functions of the X-ray wavelength, i.e., $\nu(k) = 1 - \delta(k) + i\beta(k)$. If βh is very large (i.e., the grating bars are opaque) then there is no wavelength dependence of the diffraction efficiency. The HETG gratings are designed such that the grating bars are partially *transparent* at higher energies, and so the phase shift of the X-rays through the bars (the δ term) actually enhances the efficiency at some energies. Gratings with this property are call *phased* transmission gratings.

For a quantitative look at the higher efficiency of phased gratings as compared to opaque gratings, equations 3.4 and 3.5 below show the grating efficiencies (where η is now the sum of the grating efficiencies of the $+1$ and -1 orders):

$$\eta_{opaque} = 2 \times \frac{sin^2(\frac{\pi a}{p})}{\pi^2} \tag{3.4}$$

$$\eta_{phased} = \eta_{opaque} \times [1 + e^{-2kh\beta} - 2e^{-kh\beta}cos(kh\delta)] \tag{3.5}$$

When absorption is ignored (the fully-phased case), equation 3.5 reduces to the following[68]:

$$\eta_{fully-phased} = 8 \times sin^2(\frac{kh\delta}{2}) \times \frac{sin^2(\frac{\pi a}{p})}{\pi^2} \tag{3.6}$$

From equation 3.6, it can be seen that at an optimal wavelength ($\lambda = 2h\delta$), the fully-phased grating efficiency is four times the opaque grating efficiency for this simple scalar diffraction theory. (A complete vector treatment of Maxwell's equations gives slightly different results at some energies.) At efficiencies near this one particular wavelength, partial destructive interference of the zeroth grating diffraction order occurs and the first grating diffraction orders are enhanced. The result is a range of wavelengths for which the grating efficiency is maximized.

The scalar model fits our data fairly well, even if a simple rectangular grating bar shape is assumed[56]. However, in order to match the data at the 1 per cent level, we find in general that more complex bar shape functions must be invoked. In addition, we have independent evidence, from electron microscope photographs that the bar shapes for the HETG gratings are not simple rectangles.

3.1.3 Vertex Model

The bar shape function function $z(\xi)$ can be reduced to a finite number of parameters. For example, if a rectangular bar shape is assumed, then z can be computed with two parameters, a bar width and a bar height. A more complex bar shape can be parameterized with arbitrary precision by dividing the bar into small rectangular sections.

For our modeling, the grating bar shape is parameterized as piece-wise linear, defined by the location of vertices, *e.g.*, Figures 4.8 and 4.9. The number of line segments is selectable, but there is little improvement in the quality of the fit after about 4 to 6 segments.

3.1.4 Tilted Grating Model

Another factor which makes a difference in the computed efficiencies in the various orders is the effect of tilting the grating, *i.e.*, changing the orientation of the grating surface normal with respect to the incoming X-rays. Given a grating bar cross-section, and a tilt angle (orientation of the incoming X-rays with respect to the grating plane), one can determine the grating bar shape function $z(\xi)$ from simple geometry. Since tilt and bar shape are complementary, we don't include tilt angle as a model parameter. (It is always possible to find an untilted grating with the same response as a tilted grating of an arbitrary shape. This equivalence only holds true at a given tilt angle, however. If one studies gratings over a range of angles, then one must generally use the actual bar cross-section.)

3.1.5 Trapezoidal Model

As an example of the complementarity between tilt and bar shape, consider a rectangular cross-section: When viewed at an angle, it has a trapezoidal $z(\xi)$. Moreover, the efficiency vanishes in all orders when the the grating is tilted by an angle $\theta = tan^{-1}(h/p)$, where h is the grating bar height and p is the period. (This relationship is clear because at that angle all of the X-rays incident on the grating see the same path length through the bars, hence there can be no diffraction.) Fischbach *et al.* [23] have reported on the theory and measurements of tilted rectangular gratings.

Except for a few bar cross-sections showing great symmetry, the efficiency in the positive and negative orders will be different at all but a few tilt angles. For example, Figure 3.1 shows the efficiency asymmetry in the plus and minus first orders for a trapezoidal grating at $E =$ 2.290 keV, the energy of the Mo L α line. The asymmetry at a given tilt angle is defined as $100(I_{+1}/I_{-1} - 1)$. There is order symmetry at *normal* orientation (zero degrees tilt means that the incoming X-rays are normal to the grating plane), but at very few other angles.

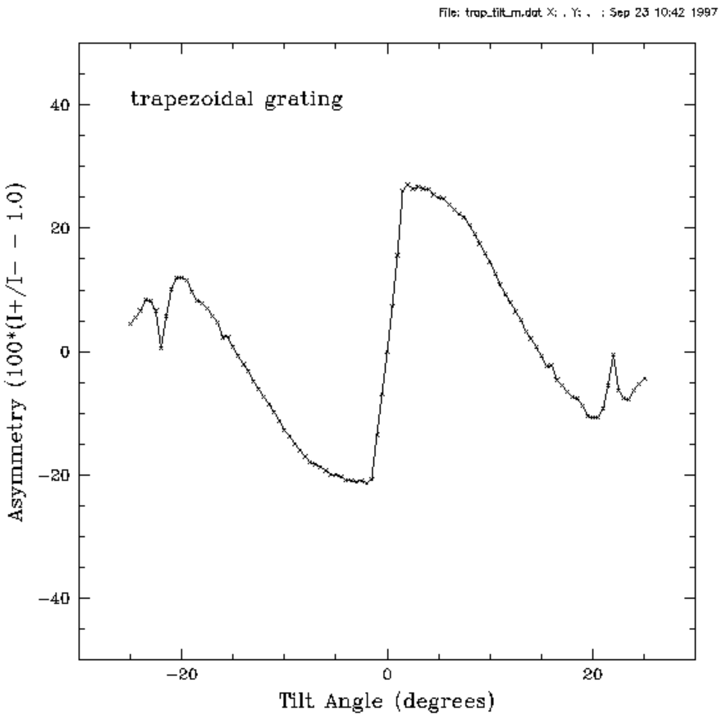

Figure 3.1: Asymetry parameter for a trapezoidal grating

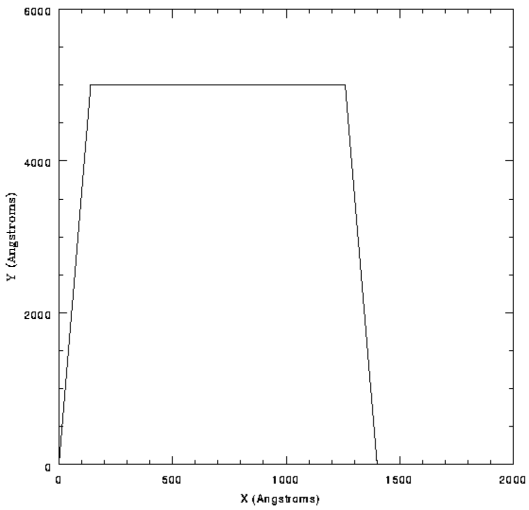

Figure 3.2: Trapezoidal bar shape assumed for the model above.

3.2 Synchrotron Measurements

3.2.1 Synchrotron Measurements Summary

The table below summarizes all the synchrotron tests which have been performed to date on HETG gratings or their prototypes.

Table 3.1: Summary of HETG synchrotron radiation tests

Date	Facility	Sample	Energy	Comments	Ref.
July '93	NSLS	HX101	2.03 - 4	preliminary tests	[55]
Nov '93	Daresbury	HX101	8.442	period variations (UL)	[55]
Jan. '94	NSLS	HX101	0.7 - 6	first tests	[56]
Feb. '94	NSLS	1Au	2.03 - 6.04	new gold optical constants	[56], in review
Jun. '94	NSLS	HA04	2.03 - 6		"
"	"	HX101	2 - 3.5		"
"	"	MA12	0.7 - 5	± 1 order assymetry	"
Feb. '95	NSLS	HX220	0.5 - 6.4	X-GEF reference grating	[47]
"	"	MX078	0.5 - 3.5	X-GEF reference grating	"
May '95	NSLS	HX220	1.05 - 1.95	X-GEF reference grating	
"	"	poly	0.4 - 1.83	poly transmission	in prep
Oct. '95	NSLS	HA2021	2.03 - 6.5	flight lot 2, dense 0&1 orders	[25]
"	"	MA1047	2.1 - 5.0	flight lot 3, dense 0&1 orders	"
Oct. '95	PTB	HA2021	0.4 - 1.9	flight lot 2	"
"	"	MA1047	0.4 - 1.5	flight lot 3	"
"	"	HA2049	0.2 - 1.5	polyimide sample, flight lot 2	in prep
"	"	MA1066	0.2 - 1.5	polyimide sample, flight lot 3	in prep
"	"	HX507	0.05 - 1.9	gold foil transmission	in prep
Mar. '96	NSLS	HD2338	2.0 - 6.4	flight lot 4, ± 1 and higher orders	in prep
"	"	MB1148	2.1 - 4.9	flight lot 9, ± 1 and higher orders	in prep
Aug. '96	ALS	poly	0.06 - .940	polyimide transmission, R. Blake	in prep
Nov. '96	NSLS	1Au	2.01 - 7.0	gold optical constants, R. Blake	in prep

3.2.2 Synchrotron Data Analysis Techniques

A complete description of the techniques employed in extracting diffraction efficiencies from synchrotron data is given in Flanagan *et al.*[25].

3.2.3 Gold Optical Constants and Edge Structure

When fitting the scalar model to the data we use the simplex technique to minimize the chi-square function. We allow all parameters to vary, except for the optical constants. There are too many optical constants (2 at each energy for gold alone), so fitting them isn't appropriate.

On the other hand, the values of the β and δ are not well-enough known to allow us to use the published values uncritically.

Our initial tests (January 1994) at the National Synchrotron Light Source (NSLS) at Brookhaven National Laboratory (BNL) indicated a significant disagreement between the Henke values for the gold optical constants[35], and those required by our tests (our results were in basic agreement with those obtained earlier by Blake *et al.*[8] from reflection studies of gold mirrors). The most noticeable feature of the disagreement was that the energies of the prominent gold M absorption edges were shifted from the tabulated amounts by as much as 40 eV.

In an effort to determine more relevant optical constants, in February, 19994 we measured the transmission of a gold foil with well-determined thickness and density in the energy range 2.03–6 keV at the NSLS using the X8A beam line. The transmission measurements yielded the complex part of the index of refraction (β) directly. We used the Kramers-Kronig relation (i.e., the dispersion relation linking δ and β) to compute the real part of the index of refraction, δ. The optical constants we required outside of this range were obtained by connecting the synchrotron-derived constants with those of Henke (at other energies) in a smooth way.

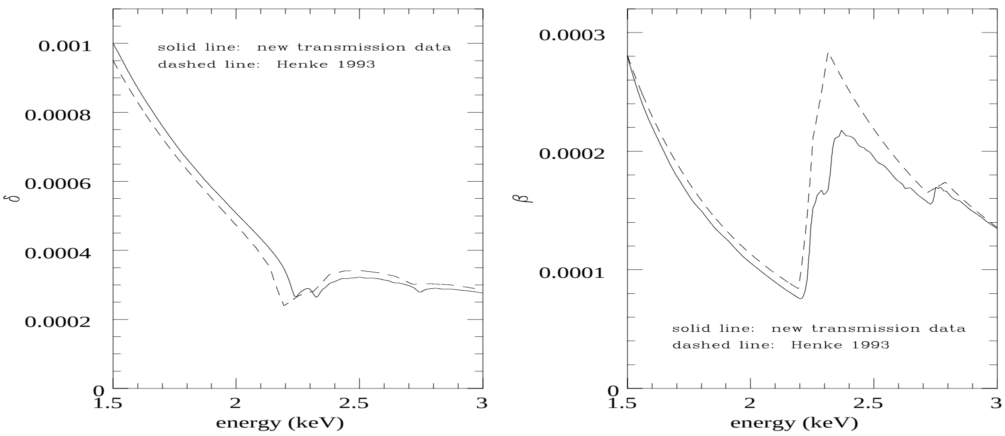

Figure 3.3: Comparison of optical constants from transmission data measured in 1994 (solid lines) to those from the Henke tables (dashed lines). The plot on the left shows the values of the real part of the index of refraction, δ, and the plot on the right shows the values of the imaginary part of the index of refraction, β.

The optical constants we determined are shown in Figure 3.3, along with the Henke *et al.*[35] values. The constants are displayed near the gold MIII, MIV, and MV edges only (1.5 keV $<$ E $<$ 3 keV). Outside this energy range, the constants we derived were in good agreement with the Henke values.

The validity of the phased, non-rectangular model and the effectiveness of updated gold optical constants for energies above 2 keV are demonstrated in Figure 3.4 , where the synchrotron-measured diffraction efficiencies, sampled over many closely-spaced energies, agree well with the

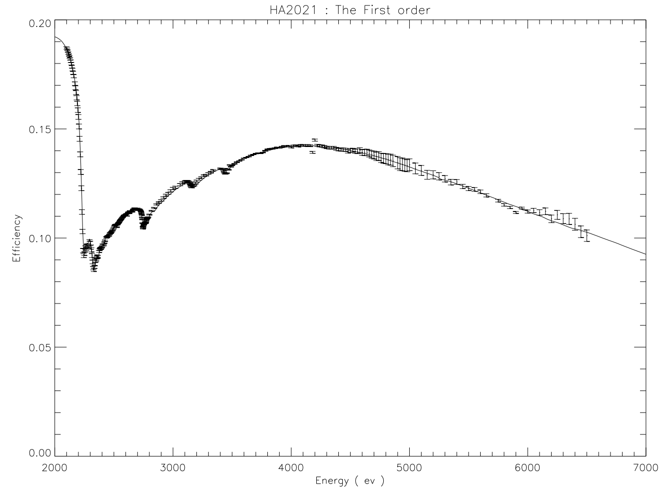

Figure 3.4: First order synchrotron data of HEG grating HA2021, overlaid with best fit model.

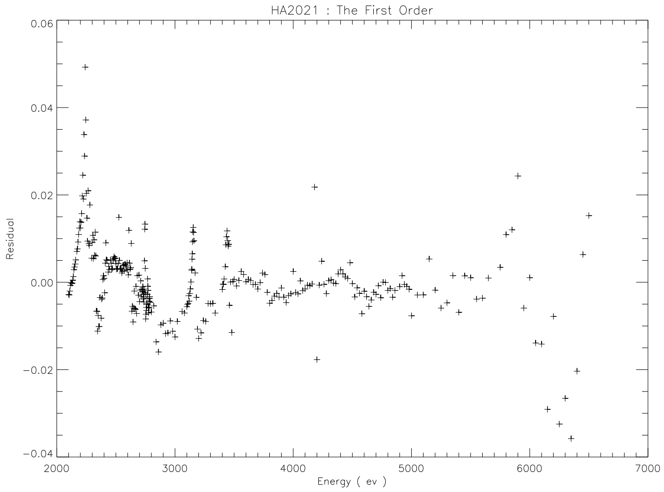

Figure 3.5: Residuals from the first order fit of grating HA2021.

modeled efficiency for a flight-batch HEG grating. The residuals are shown in Figure 3.5 (only the first order data were used in the fit). The excellent agreement of the model with the data at the gold M edges is seen in better detail in Figures 3.6 and 3.7 for a flight-batch MEG grating. Note that the residuals at the gold edges are generally within 1%.

There have been subsequent tests of gold transmission in 1996 by Richard Blake at NSLS and by Tom Markert at PTB (at BESSY). Blake's data above 2 keV agree well with the 1994 measurements. Analysis of the PTB gold data (1.9 keV and below) is underway.

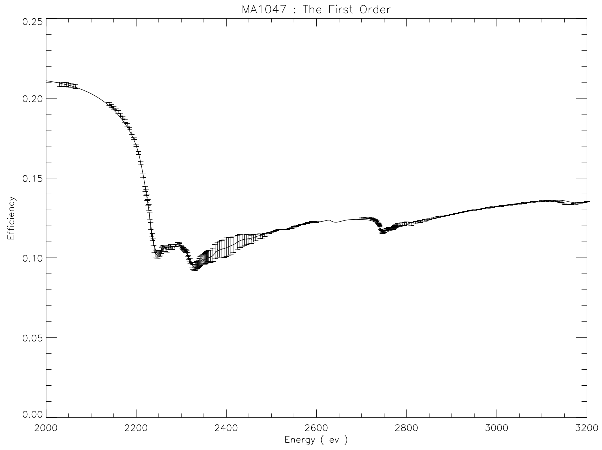

Figure 3.6: First order synchrotron data of MEG grating MA1047, overlaid with best fit model.

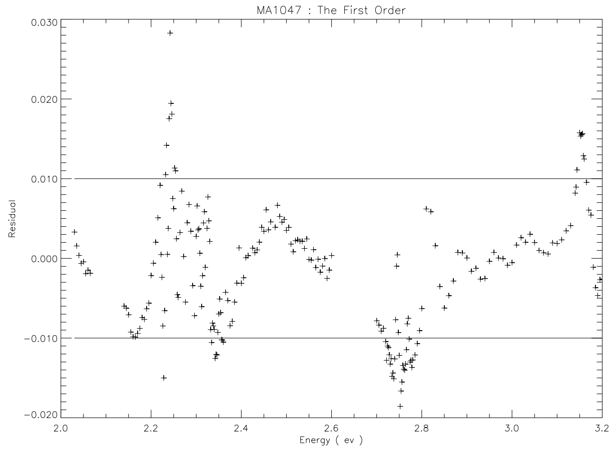

Figure 3.7: Residuals from the first order fit of grating MA1047. The horizontal lines are at ±1%.

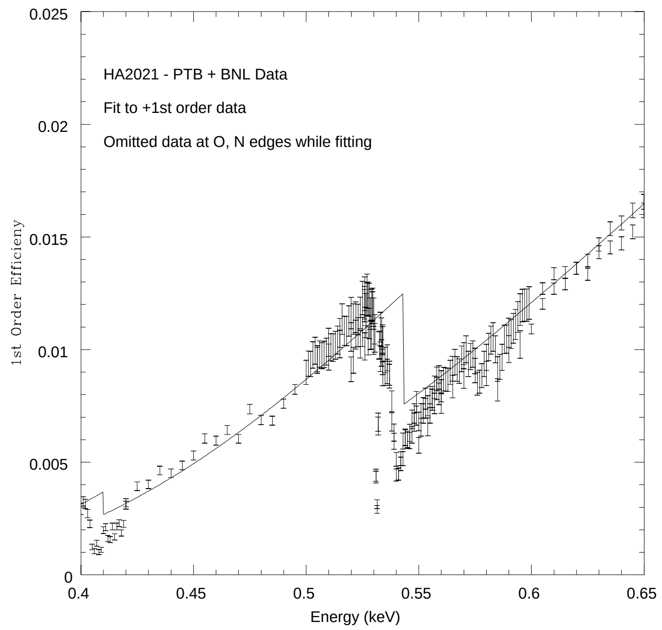

Figure 3.8: Data and best-fit model of grating HA2021 at polyimide and Cr edges, with Henke constants used in the model.

3.2.4 Polyimide and Chromium Optical Constants and Edge Structure

Measurements of the gold optical constants have enabled the detailed gold edge structure to be well represented. A similar approach has been taken toward modeling the C, N and O edges of the polyimide. We have tested samples of polyimide from MEG and HEG flight batches at the radiometry laboratory of the PTB at BESSY[25]. These data show that there is considerable edge structure at the C, N and O edges in our polyimide. Our approach is to model the polyimide assuming the chemical formula ($C_{22}H_{10}O_4N_2$) and nominal density (1.45 g/cm^3) for the polyimide formulation we use (Dupont 2610). In prior modeling, the optical constants for the polyimide support film and the chromium plating base have been taken from Henke, Gullikson and Davis[35]. This modeling, however, provided an unacceptable fit at the edges, as shown in Figure 3.8. In this figure are seen oxygen, nitrogen and chromium edges, as well as EXAFs: all are inadequately represented by the model. The residuals are given in Figure 3.9, and exceed 200% at the C and N edges. Just below 600 eV are seen edge residuals of about 20% from Cr L. Similar results have been found for the MEG grating MA1047. Taking the model as a whole, the polyimide edges exhibit the worst discrepancies between our physical model and the data overall.

In order to refine the optical constants for our polyimide at the C, N and O edges, we used the PTB data for the two flight batch polyimide samples. We began by finding a best-fit thickness for each of the (MEG and HEG) polyimide samples assuming Henke optical constants and fitting over the edge-free energy range 0.6 to 1.6 keV. For each sample, an effective absorption coefficient μ is obtained assuming $T = e^{-\mu t}$ where **t** is the thickness in microns and T is the transmission through the polyimide foil. The final value for μ is taken to be the average value of the HEG and MEG μ, between 272 eV and 875 eV, smoothly joined to the Henke values outside this region. In addition, we smoothed the derived μ in the carbon edge region between

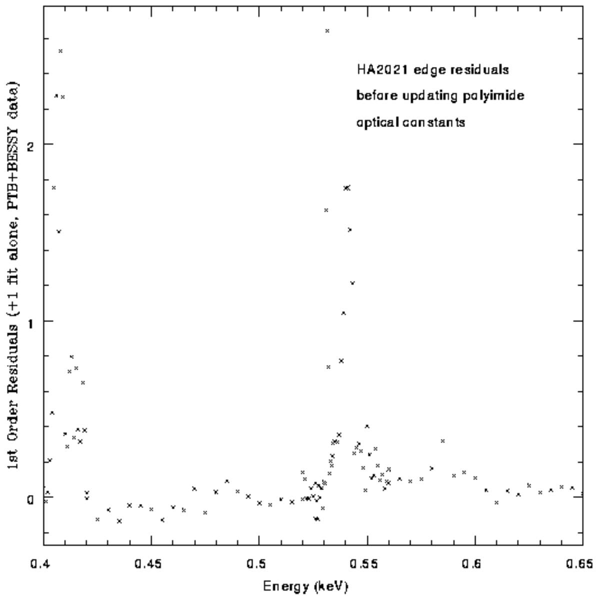

Figure 3.9: Residuals for grating HA2021 at polyimide and Cr edges, where Henke constants have been used.

288.8 eV and 300.99 eV because low counting statistics otherwise introduce a jittery structure there. Note that the 1982 Henke constants for carbon were employed as these were found to agree better with our data and have been shown in independent tests by the HRC instrument team as the the better choice. The discrepancy between the average μ and the μ extracted from the data provides a first estimate of the error on μ.

This technique does not adequately accomodate certain systematic errors. In particular, synchrotron beamlines have notorious difficulty with measurements near the carbon edge. (Carbon buildup on the monochromator absorbs much of the incident flux, heightening the relative percentage of contaminant energies, and giving low overall counting statistics.) The gratings tests at BESSY did not cover the carbon edge, and only one polyimide sample provided an estimate for μ. Richard Blake tested a polyimide sample supplied by Mark Schattenburg (of the HETG team) and at ALS (Advanced Light Source at the Lawrence Berkeley National Laboratory) in 1996. He found a best-fit ρt of 124.25 $\mu g/cm^2$. Assuming a density of 1.45 g/cm^3, he derived a value for μ/ρ in a similar manner as has been described with regard to the BESSY data. After conversion to comparable units, a comparison of our μ/ρ, Henke's and Blakes is given for the nitrogen edge in Figure 3.10. In general, we found good agreement between the two data sets, except at the carbon edge. This close agreement between data sets generally confirms the detailed edge structure and magnitudes of the absorption coeficients we have derived. The independent ALS measurements will be used to provide a second estimate of errors on the absorption coefficients. Measurements taken on the BNL beamline X8A with the multilayer monochromator are of insufficient resolution to reproduce the details of the edge structure.

In order to accomodate the Cr edge structure below 600 eV, we employed a different approach since we do not have transmission tests of a Cr filter of known thickness. We took zero order grating data from MA1047 (measured at BESSY) and fit it assuming a fixed thickness of Cr (55 Åfrom fabrication measurements). We assumed that the absorption features seen at 577 eV and 586 eV could be modeled as a perturbation on the absorption coefficient as derived from the Henke constants.

The new Cr and polyimide results have been incorporated into the file optical-constants.981023. Realistic errors of the new optical constants are probed by applying these constants to fit an independent data set. This is provided by BESSY measurements on the two gratings, HA2021 and MA1047, in the case of the polyimide constants, and by HA2021 and first order MA1047 in the case of the Cr constants. (No other high-resolution grating measurements in this energy range are available from other synchrotron facilities.) The data and best-fit model obtained from fitting the first order of HA2021 are shown in Figure 3.11. The residuals are given in Figure 3.12. In each, we have excluded energies below 600 eV from the fitting process and we have fixed the thickness of the chromium layer to the fabrication measurement. Note that the residuals are reduced by a factor of 3-5 at the C, N and Cr edges relative to the former fitting. The new optical constants file, which improves the edge treatment, will be incorporated into an upcoming revision of grating efficiencies but hasn't been implemented yet.

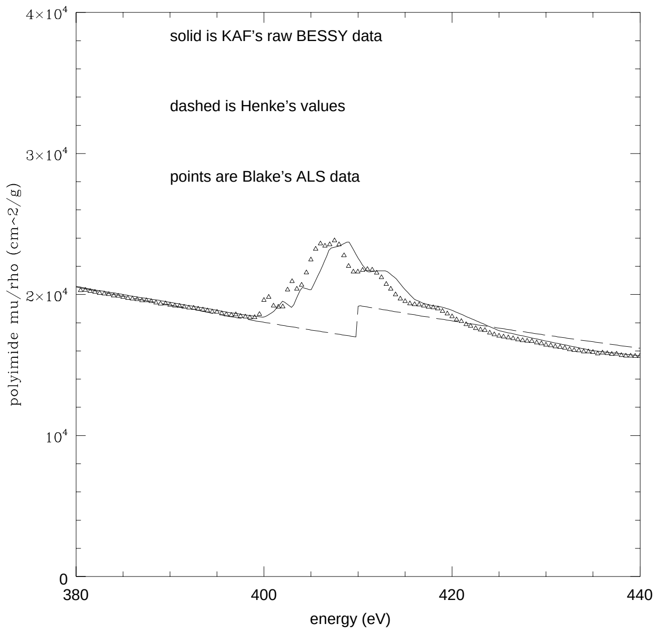

Figure 3.10: A comparison of absorption coefficients at the nitrogen edge shows good agreement between ALS and PTB (BESSY) data sets, and strong departure from the Henke values. There is evidently a small energy offset between the two data sets.

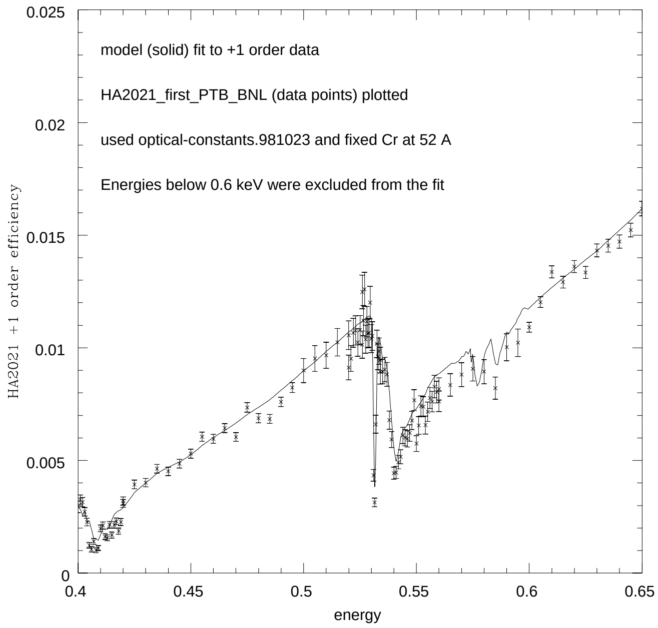

Figure 3.11: Data and best-fit model of grating HA2021 at polyimide and Cr edges, with optical-constants.981023 used in the model.

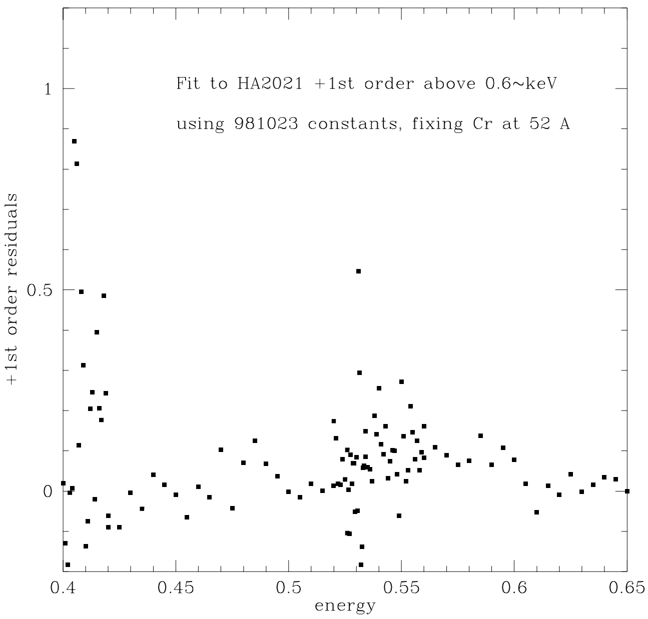

Figure 3.12: Residuals for grating HA2021 at polyimide and Cr edges, where optical-constants.981023 has been used.

3.2.5 Reference Grating Measurements

Although these data provide estimates as to the validity of our grating model, synchrotron tests are impractical to use for more than a few gratings. For the full set of flight gratings, the model parameters are determined from laboratory measurements on each grating element, using a standard (electron impact) type X-ray source and a few X-ray lines in MIT's X-Ray Grating Evaluation Facility (X-GEF). Gratings that have been tested at the synchrotron are used as transfer standards in each X-GEF test, to minimize systematic errors and allow normalization against a known efficiency.

Two gratings, HX220 and MX078, were tested early in the program at a synchrotron (Markert *et al.*[47]). These are used as transfer standards in X-GEF testing; each X-GEF efficiency measurement is performed with an analogous measurement on the reference grating. Based on the assumption that the diffraction efficiency of the reference grating is correctly known at that energy, we obtain the efficiency of the test grating at the measurement energy. From measurements made at 5 or 6 energies in the laboratory, we then estimate the best-fit parameters (bar shape, gold thickness, space-to-period ratio) for the test grating and generate a model for its diffraction efficiency at all appropriate AXAF energies.

Figures 3.13 and 3.14 illustrate the quality of the model fit to the synchrotron data for the HX220 reference grating. Figures 3.15 and 3.16 show the data and fit for the reference grating MX078. These fits used both the first order and zeroth order data.

Tilt tests were performed in X-GEF on the two reference gratings. Figure 3.17 plots the asymmetry of MX078 versus angle at the Mo L line. MX078 exhibits no substantial asymmetry (confirming results found at Brookhaven). Figure 3.18 shows the asymmetry parameter found for HX220, the HEG reference grating. For reference, we have overlaid the results found in a tilt test performed at Brookhaven, which shows substantial agreement. The modeling for HX220 is discussed in Markert, *et al.*[47]

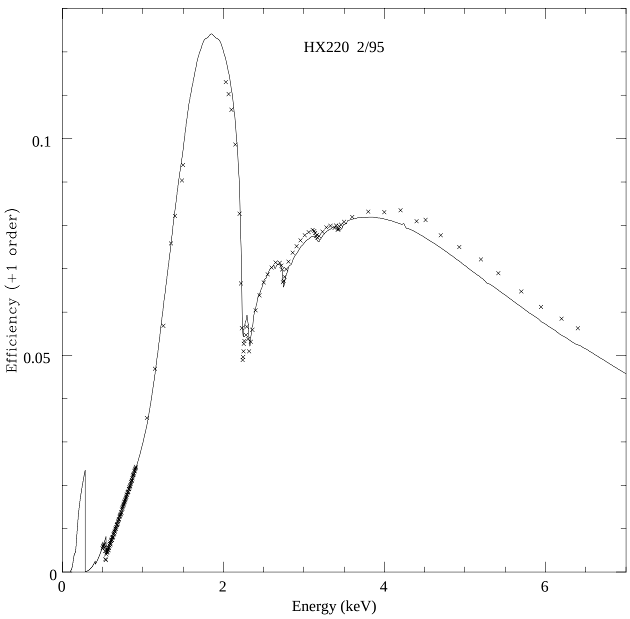

Figure 3.13: Data and best-fit model of reference grating HX220.

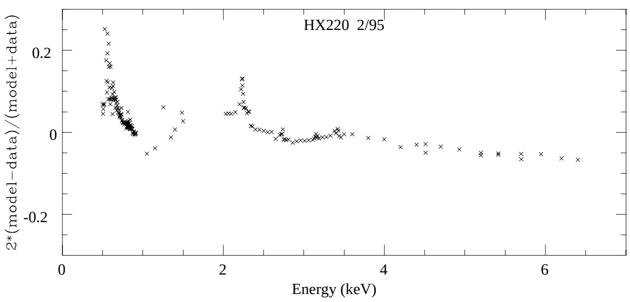

Figure 3.14: Residuals for reference grating HX220.

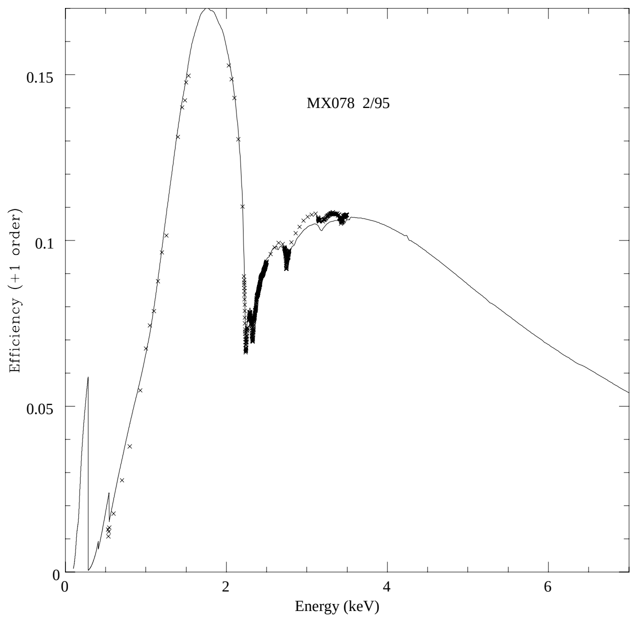

Figure 3.15: Data and best-fit model of reference grating MX078.

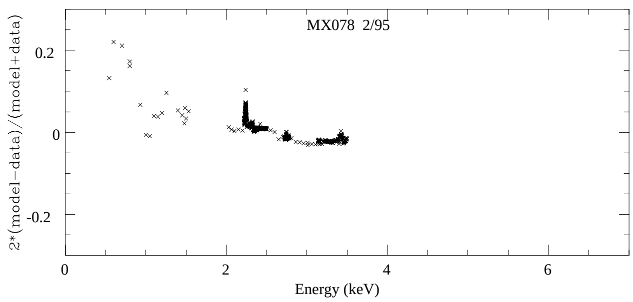

Figure 3.16: Residuals for reference grating MX078.

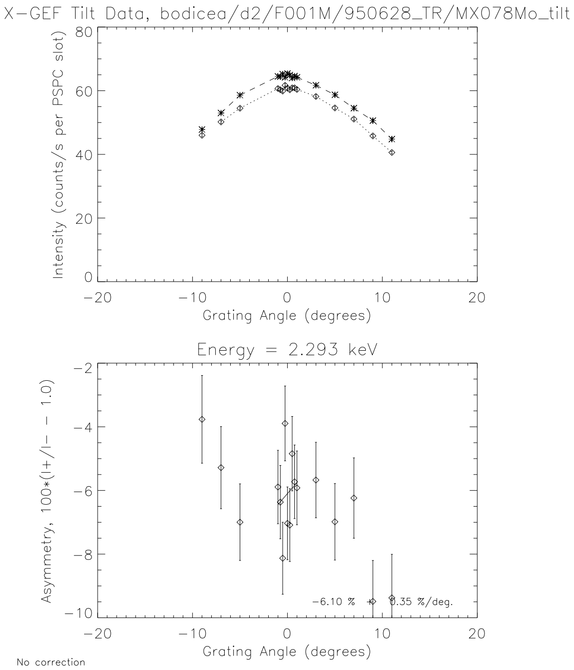

Figure 3.17: The X-GEF tilt test data for MX078 confirms the synchrtron result of a minimal tilt-induced asymetry.

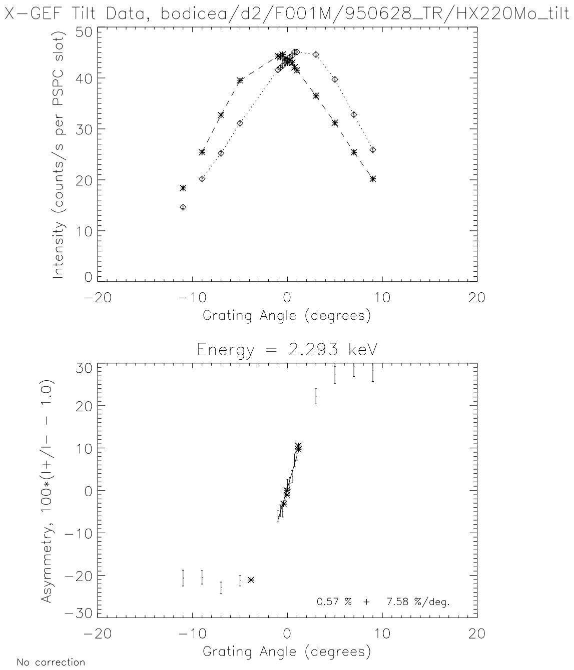

Figure 3.18: The X-GEF tilt depencance for HX220 agrees with measurements made in a tilt test at NSLS, overlaid(*). An angular offset if 1.15 degrees has been added to the NSLS measurements.

3.2.6 Error Estimates for X-GEF Predictions of Grating Efficiency

Four gratings have been cross-tested both at X-GEF (using standard flight testing and analysis prodecures including the reference gratings to normalize their efficiencies) and at the synchrotron. By comparing the X-GEF derived efficiency model with the synchrotron measurements, we have an estimate of the errors implicit in using X-GEF to predict the efficiencies for each grating facet. The residuals between the X-GEF generated model and the synchrotron data are shown in Figure 3.19 and 3.20. In effect, this provides an *upper limit to the errors of our subassemby efficiency predictions*, because a large strip of the reference grating is in fact illuminated in each X-GEF test, and the diffraction efficiency of this strip is (incorrectly) assumed to have the synchrotron reference efficiency. Only a small portion of the reference grating was actually tested at the synchrotron and it is only this small portion which should actually be assigned the reference efficiency. Therefore, the assignment of this fixed efficiency to a much larger area of the reference grating is incorrect. Tests have been done to cross-normalize the strip efficiency in comparison to the confined area for each grating, but the results have not been included yet.

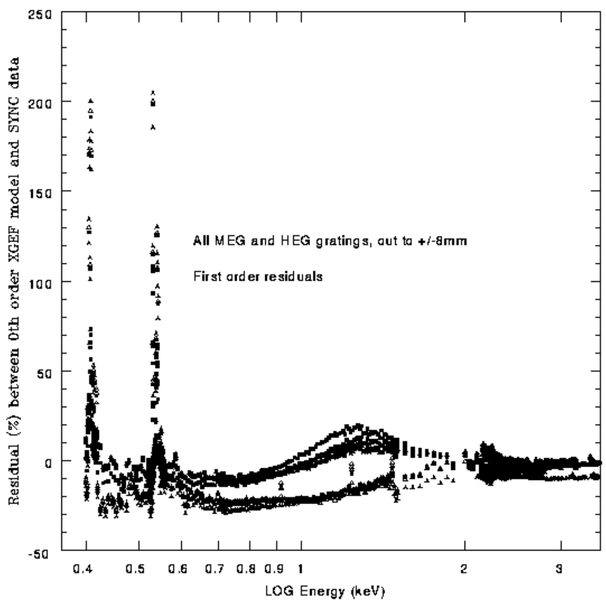

Figure 3.19: Residuals between first order X-GEF predictions and synchrotron data. The large residuals at the N and O edges should be reduced when new X-GEF predictions are generated assuming updated (October, 1998) optical constants.

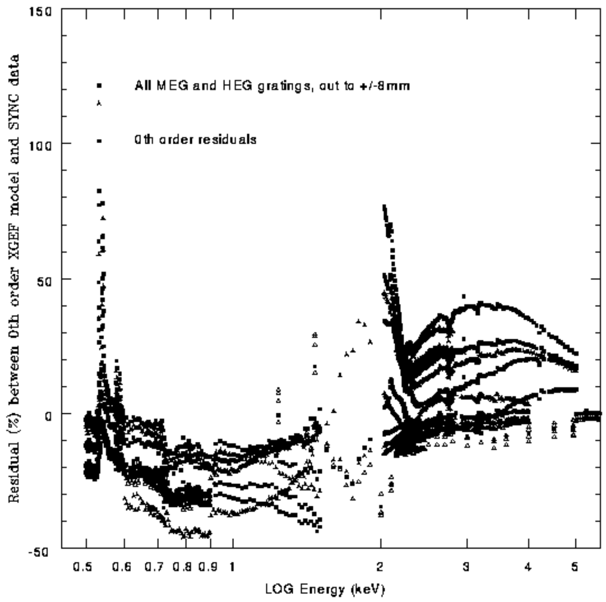

Figure 3.20: Residuals between 0th order X-GEF predictions and synchrotron data. Edge residuals between 0.5 and 0.6 keV should be reduced when predictions are generated assuming updated (October, 1998) optical constants.

3.2.7 Synchrotron Analysis Status

1. The non-rectangular phased model is used in the X-GEF-modeling technique, its errors estimated and it has been documented in the literature.

2. Updated gold optical constants are also employed in this modeling. Recent tests on gold confirm our model above 2 keV, but BESSY data below 1.9 keV await analysis before the gold constants at lower energies can be checked.

3. Reference gratings have been assigned efficiencies based on early synchrotron tests. These values need to be examined and errors attached, reflecting increased knowledge of the synchrotron beamline systematics obtained in subsequent tests. The biggest considerations are:

   - Reconsideration of the cross-calibration techniques (high priority)
   - Careful examination of the multilayer data (below 2.03keV) which may contain low-energy contamination. (high priority)
   - Applying wing corrections and error bars.

4. Reference grating efficiencies are applicable to a small spatial region of each reference grating, but have been assumed for large regions in X-GEF tests. Cross-normalization tests have been performed in X-GEF (in a test procedure labeled BRLONG), so that efficiencies over a large strip can be normalized to the central section, and a proper reference efficiency can be assigned for the large test strip. This needs to be completed.

5. The results of the above projects will provide new efficiencies and errors for the reference gratings as used in X-GEF tests. These improved reference efficiencies can then be transferred to the flight grating measured efficiencies.

6. New optical constants have been obtained that treat the C, N and O edges of polyimide and strong chromium edges around 577 and 586 eV. Include any appropriate changes from examining gold data and finalize. Attach error bars derived from comparisons among independent measurements. Supply polyimide constants, as required, to ACIS and HRC groups for their filter modeling.

7. Repeat model fits for flight gratings incorportaing best optical constants and incorporating revised reference grating efficiencies.

8. Finish analysis of NSLS tests of gratings HD2338 and MB1148, to examine ratios of higher orders to first order. Compare these results with apparent systematic behavior of higher orders found with HETG + HRC-I tests at XRCF[26].

9. We have looked for evidence of scattering in synchrotron data, and find it to be qualitatively consistent with modeling describing the scattering noted at XRCF[16].

3.3 Scattering Model

Objective: Understand and model the "anomalous scatter" seen in XRCF tests of the HEG gratings, Section 6.6.

Publication(s): Davis *et al.* [16]

3.3.1 Introduction

XRCF tests of the HEG gratings showed anomalous scattering of monochromatic radiation, in particular the gratings showed events with significant deviations from the integer grating orders and the events were concentrated along the dispersion direction, Section 6.6 and Marshall *et al.* [48].

In this section, we present a general overview of grating scatter as a result of fluctuations in the grating bar geometry. The measured HEG grating scatter is shown to be consistent with what one expects from scatter due to deviations in the grating bar geometry from perfect bars. For the purposes of modeling, a rectangular bar model is adopted and bar parameters are deduced via fitting the model to the scattering data. The correlations deduced from this model lead to a simple physical picture of grating bar fluctuations where a small fraction of the bars, e.g., 1 in 200 are leaning.

We treat the problem of scattering from a disordered diffraction grating, and from first principles arrive at an equation for the probability distribution of scatter from such a grating. Without making any reference to a specific geometric model for the grating bar shapes, we show that the anomalous scattering observed at XRCF (e.g., see Figure 3.21) shares many of the features that one would expect to be produced as a result of grating disorder. In particular, the strong peaks that appear symmetrically about the various diffraction orders can be explained as a natural consequence of one or more correlations between neighboring bars with a correlation length that is characterized by the width of the peaks. The correlation length is estimated to be roughly three grating periods.

A more detailed description of the correlations based on a rectangular model for the bar shapes is presented in the section 3.3.5. Although the rectangular model has been shown to be inadequate for modeling the grating efficiency to the one percent calibration goal[47], it performs well at the ten to twenty percent level. Its most redeeming feature is its simplicity, which allows many of the calculations to be performed analytically. Within the context of this model, expressions for the correlations and the scattering probability are derived and then fitted to the experimental data. The resulting fit, while not perfect, does reflect many of the salient features of the data, although the resulting effective rectangular parameters are somewhat larger than the values implied by modeling of the grating efficiencies, Figure 1.3.

In the final section we present a discussion of the correlations as deduced from the modeling. Based upon the form of the correlations, a physical picture of the gratings emerge in which a small fraction (e.g., 1 in every 200) of the grating bars are leaning. Finally, the major results of this section are summarized and future modeling improvements are suggested.

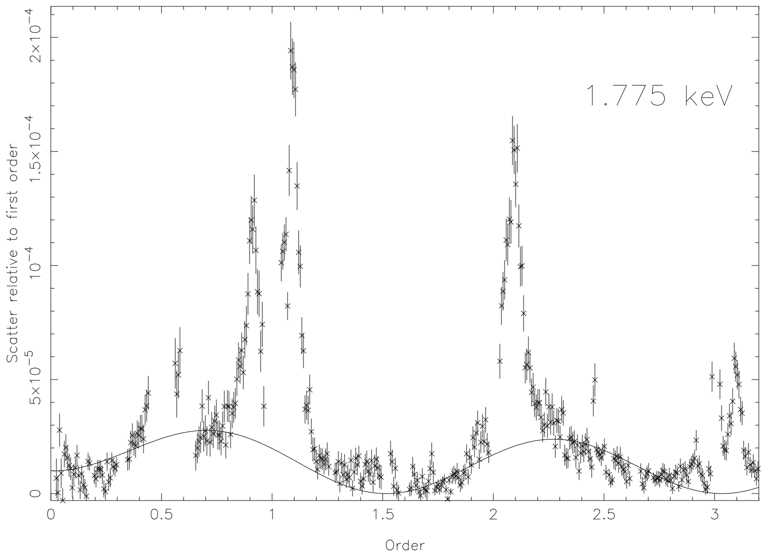

Figure 3.21: Measured HEG scatter at 1.775 keV. The scattering-per-bin normalized to the first-order intensity is plotted versus diffraction order. The solid curve is the best fit to this data using a simple rectangular grating model with no bar-to-bar correlations.

3.3.2 General Formulation

Consider a diffraction grating composed of N lines, or bars, with period d, and a photon with wave number $k = 2\pi/\lambda$ incident upon the grating. It follows from Huygen's principle that the probability for scattering into an angle between θ and $\theta + \mathrm{d}\theta$ with respect to the normal of the grating is given by

$$p(k,s)\mathrm{d}s = \frac{kd}{2\pi N}\left|\sum_{j=0}^{N-1} e^{ijksd} F_j(k,s)\right|^2 \mathrm{d}s\ , \tag{3.7}$$

where $s = \sin\theta$ and the *structure factor* $F_j(k,s)$ is defined by

$$F_j(k,s) = \frac{1}{d}\int_0^d \mathrm{d}x\ e^{iksx + i\phi_j(k,x)}. \tag{3.8}$$

The shape and composition of an individual grating bar determines the complex phase shift $\phi_j(k,x)$ that, in general, depends upon energy and, possibly, the polarization of the photon. Assuming the validity of scalar diffraction theory, and neglecting reflection and refraction, the phase shift can be written in the form

$$\phi_j(k,x) = -k(\delta - i\beta)z_j(x), \tag{3.9}$$

where δ and β are energy dependent functions related to the dielectric constant of the grating bars. The function $z_j(x)$ represents the path length of the photon as it passes though the jth grating bar; it is sometimes called, rather loosely, the "grating bar shape", and more rigorously, the "path-length function".

In general, the structure factor $F_j(k,s)$ will vary with the grating bars because the "bar shape" will vary from bar to bar. Since an exact computation of the scattering probability would require complete knowledge of all the bar shapes, and since there are millions of bars that contribute to the scattering, we must resort to a statistical means of computing Eq. 3.7. This is completely analogous to the situation in statistical physics where one deals with systems that consist of large numbers of degrees of freedom, and whose complete characterization requires a knowledge of the initial conditions for each degree of freedom. These problems are treated statistically where one introduces the notion of an ensemble of macroscopically identical systems and makes an ergodic hypothesis that at any given instant the microscopic state of the system is represented by one of the systems in the ensemble. Hence the assumption of ergodicity allows one to compute the time average of a macroscopic quantity by averaging that quantity over the ensemble. In a similar vein we shall introduce the idea of an ensemble of gratings and make the assertion that the observed scattering does not depend upon the exact "microscopic" state of the grating, but that it is an indicator of the "macroscopic" state. In other words, we shall assume that the scattering is a macroscopic property of the ensemble and may be computed via

$$p(k,s)\mathrm{d}s \;= \frac{kd}{2\pi N}\left\langle \left| \sum_{j=0}^{N-1} e^{ijksd} F_j(k,s) \right|^2 \right\rangle \mathrm{d}s\ , \tag{3.10}$$

where $\langle\cdot\rangle$ denotes averaging over the ensemble. The specification of the ensemble involves knowing the probability for a particular configuration of grating bars, denoted by the ordered set of bar shapes $\{z_j\}$. Let this probability be represented by the probability density $\mathcal{P}(z_0, z_1, \ldots, z_{N-1})$ such that the ensemble average of some function $f(z_0, \ldots z_{N-1})$ is given by [1]

$$\langle f(z_0,\ldots,z_{N-1})\rangle = \int \mathcal{D}z_0(x)\cdots\mathcal{D}z_{N-1}(x) f(z_0,\ldots,z_{N-1})\mathcal{P}(z_0,\ldots,z_{N-1}). \tag{3.11}$$

Furthermore, we shall assume that the ensemble is such that $\langle f(z_j)\rangle$ is independent of j, and that $\langle f(z_j, z_l)\rangle$ depends only upon the difference $j-l$. For obvious reasons, a probability distribution with these properties is said to be *homogeneous* or *stationary*[73].

With the assumption of a homogeneous probability distribution for bar shapes, denote the ensemble averaged structure factor by

$$\bar{F}(k,s) = \langle F_j(k,s)\rangle \tag{3.12}$$

and define $f_j(k,s)$ to be the deviation of the jth bar from this value via

$$F_j(k,s) = \bar{F}(k,s) + f_j(k,s). \tag{3.13}$$

Substituting the above definitions into Eq. 3.10 yields for the probability density

$$p(k,s) = \frac{kd\sin^2(\frac{1}{2}Nksd))}{2\pi N\sin^2(\frac{1}{2}ksd)}|\bar{F}(k,s)|^2 + \frac{kd}{2\pi N}\sum_{j,l} e^{iksd(j-l)}\langle f_j f_l^*\rangle. \tag{3.14}$$

For very large N, the first term goes to zero like $1/N$ except when ksd is a multiple of 2π where it becomes proportional to N. In fact, one can show that the factor involving N in first term is a representation of a series of delta functions:

$$\frac{kd\sin^2(\frac{1}{2}Nksd)}{2\pi N\sin^2(\frac{1}{2}ksd)} = \sum_n \delta_N(s - \frac{2\pi n}{kd}). \tag{3.15}$$

[1] Since the bar shape $z_j(x)$ is a function, the integrals in this equation are functional integrals and the symbol $\mathcal{D}z(x)$ is called the *Weiner measure.* See the book by Feynman and Hibbs[22] for a simple introduction to functional integration. Alternatively, one can view such an integral as a multiple integral over the parameters defining a shape, e.g., the bar width and height for a rectangular bar.

This equivalence allows the probability density to be written

$$p(k,s) = |\bar{F}(k,s)|^2 \sum_n \delta_N(s - \frac{2\pi n}{kd}) + \frac{kd}{2\pi N} \sum_{j,l} e^{iksd(j-l)} \langle f_j f_l^* \rangle. \tag{3.16}$$

Thus, the first term represents the familiar interference pattern that consists of a series of sharp peaks, weighted by $|\bar{F}(k,s)|^2$, whose height varies with N. The peaks occur at values of ksd that are multiples of 2π, or equivalently when

$$n\lambda = d \sin\theta, \tag{3.17}$$

which is the familiar grating equation. The second term is the scattering term and is more complicated. Superficially, it appears to vanish in the limit of a large number of bars; however, owing to the double sum (hence N^2 terms), this is not necessarily true.

The quantities $\langle f_j f_l^* \rangle$ represent correlations between the various grating elements. If the shape of each grating bar element is independent of the others, then $\langle f_j f_l^* \rangle$ vanishes except when $j = l$. More explicitly, if no correlations exist between the fluctuations of the grating bars then

$$\langle f_j f_l^* \rangle = \langle |f_j|^2 \rangle \delta_{jl}. \tag{3.18}$$

If there are correlations between the various grating bars, then Eq. 3.18 is not correct. We make the assumption that if any correlations are present, then they have a short range. This is really an assumption about the fabrication method, but one could imagine the presence of long range correlations from e.g., a holographic fabrication process in which a non-monochromatic light source would create a beating effect. Similarly, for a "ruled" grating, the mechanical system could introduce periodic long range correlations. Nevertheless, we shall assume that $\langle f_j f_l^* \rangle$ is zero for $|j-l|$ greater than some number M. For example, if $M = 1$, then only nearest neighbor correlations may be present. If $M \ll N$, then one may neglect edge effects in the sum and write the scattering term in Eq. 3.16 as

$$\frac{kd}{2\pi N} \sum_{j=0}^{N-1} \sum_{m=-M}^{M} e^{imksd} \langle f_j f_{j+m}^* \rangle. \tag{3.19}$$

Since we have assumed that the ensemble governing the probability distributions is homogeneous, by definition we know that the correlations are translation invariant, i.e., $\langle f_j f_{j+m}^* \rangle$ does not depend upon j. Hence, the scattering term reduces to

$$\frac{kd}{2\pi} \sum_{m=-M}^{M} e^{imksd} c_m(k,s), \tag{3.20}$$

where c_m has been defined by

$$c_m(k,s) = \langle f_j(k,s) f_{j+m}^*(k,s) \rangle. \tag{3.21}$$

Using the property that $c_{-m} = c_m^*$, which follows from the definition of c_m, and separating out real and imaginary parts, it follows that Eq. 3.16 may be written

$$\begin{aligned} p(k,s) =& |\bar{F}(k,s)|^2 \sum_n \delta_N(s - \frac{2\pi n}{kd}) + \frac{kd}{2\pi} c_0(k,s) \\ &+ \frac{kd}{\pi} \sum_{m=1}^{M} \Big\{ \mathrm{Re}[c_m(k,s)] \cos(mksd) - \mathrm{Im}[c_m(k,s)] \sin(mksd) \Big\}. \end{aligned} \tag{3.22}$$

This equation shows that the intensity pattern will consist of sharp diffraction peaks on top of a weak but diffuse scattering background. The actual angular dependence of the diffuse scattering will depend upon the precise nature of the correlations and upon the correlation length given by M. Nevertheless, this equation permits us to make several observations about the scattering without reference to a detailed model of the grating bar shapes.

First of all, note that if the correlations $c_m(k,s)$ are slowly varying functions of s, then the scattering will be quasi-periodic with a period of $2\pi/kd$. That is, the scattering will roughly repeat itself between diffraction orders. The scattering data shown in Figure 6.19 appears to share this feature. For example, strong scattering peaks appear just to the right of the first, second, and third diffraction orders. In addition, there is a peak just to the left of first order and there appears to be some evidence for peaks just to the left of the second and third orders, although the existence of the peak at the left of second order is questionable. On the other hand, the fact that the scattering is not strictly periodic is just an indication that $c_m(k,s)$ depends upon s.

3.3.3 Displacement Variations

One might think that since the scattering is relatively weak near zeroth order with no strong peaks in that region, the apparent quasi-periodicity reflected in the data around first, second, and third orders is coincidental. However, an important prediction of Eq. 3.22 is that for fluctuations involving simple displacements of the grating bars, there can be no scattering near zeroth order. In fact, this is a well known result from the theory of X-ray diffraction from crystals[78]. To prove this in the context of a diffraction grating, consider a model of N grating bar shapes that differ from one another only by a shift, or displacement from their ideal lattice positions. That is, the path-length function for the jth bar is assumed to be given by $z_j(x) = z(x + a_j)$ where a_j denotes the shift of the bar from its ideal position in the unit cell. Furthermore, assume that $z(x)$ is non-zero only for values of x such that $|a_j| \le x \le d - |a_j|$ for all j. Physically, this means that the center of the grating bar whose shape is described by $z(x)$ lies near middle of the cell. Then, the structure factor F_j for the jth unit cell can be written

$$\begin{aligned} F_j(k,s) &= \frac{1}{d}\int_0^d \mathrm{d}x\; e^{iksx + i\phi(x+a_j)} \\ &= \frac{1}{d} e^{-iksa_j} \int_{a_j}^{d+a_j} \mathrm{d}x\; e^{iksx+i\phi(x)} \\ &= \frac{1}{d} e^{-iksa_j} \left(\int_0^d + \int_d^{d+a_j} - \int_0^{a_j} \right) \mathrm{d}x\; e^{iksx+i\phi(x)}. \end{aligned} \tag{3.23}$$

With the assumption that $z(x)$, and hence $\phi(x)$, vanishes for $x < |a_j|$ or for $x \ge d - |a_j|$, the latter two integrations can be performed with the result

$$F_j(k,s) = e^{-iksa_j} F(k,s) + \frac{1}{iksd}(1 - e^{-iksa_j})(e^{iksd} - 1). \tag{3.24}$$

Here, $F(k,s)$ has been defined

$$F(k,s) = \frac{1}{d}\int_0^d \mathrm{d}x\; e^{iksx+i\phi(x)}. \tag{3.25}$$

From this, it trivially follows from Eq. 3.12, that

$$\bar{F}(k,s) = \langle e^{-iksa_j} \rangle F(k,s) + \frac{1}{iksd}(e^{iksd} - 1)(1 - \langle e^{-iksa_j} \rangle) \tag{3.26}$$

and we also deduce from Eq. 3.13 that

$$f_j(k,s) = \left[e^{-iksa_j} - \langle e^{-iksa_j}\rangle\right]\left[F(k,s) - \frac{1}{iksd}(e^{iksd}-1)\right]. \tag{3.27}$$

Thus, from this equation it is immediately clear that a model of grating bar *fluctuations consisting of pure displacements produces no scattering in the immediate vicinity of zeroth order.* This result is quite general since no further assumptions were made about about the actual shape of the grating bars.

To see the impact of these fluctuations on the diffraction orders, assume that the shift parameters a_j are independently Gaussian distributed with a mean of zero and a variance of σ^2. For such a distribution, one can show that

$$\langle e^{-i2\pi n a_j/d}\rangle = e^{-\frac{1}{2}(2\pi n\sigma/d)^2} \tag{3.28}$$

from which it follows

$$|\bar{F}(k,s_n)|^2 = |F(k,s_n)|^2 e^{-(2\pi n\sigma/d)^2}, \tag{3.29}$$

where $s_n = 2n\pi/kd$ is the value of s at the nth diffraction order. This equation explicitly shows that the fluctuations reduce the power in the diffraction orders, as one would expect from considerations of flux conservation.

3.3.4 Bar Geometry Variations

The geometry of the jth grating bar may be specified by a number of geometric quantities. Let the μth such quantity for the jth bar be denoted by $\xi_\mu^{(j)}$. For example, a rectangular grating bar may be specified by three quantities: the width (ξ_1), height (ξ_2), and displacement (ξ_3). The structure factor F_j will be a function of these quantities and indicated symbolically by $F_j(k,s,\xi)$. Let $\Delta\xi_\mu^{(j)}$ be the deviation of the μth parameter from its mean, i.e.,

$$\xi_\mu^{(j)} = \langle \xi_\mu^{(j)}\rangle + \Delta\xi_\mu^{(j)}. \tag{3.30}$$

Assuming that the fluctuations $\Delta\xi_\mu^{(j)}$ are small, we can approximate the structure factor by

$$F_j(k,s,\xi) = F(k,s,\langle\xi\rangle) + \sum_\mu \frac{\partial F}{\partial \xi_\mu}\Delta\xi_\mu^{(j)}, \tag{3.31}$$

where $F(k,s,\langle\xi\rangle)$ is independent of j by virtue of the assumed homogeneity of the ensemble. It then follows from Eq. 3.13

$$f_j(k,s,\xi) = \sum_\mu \frac{\partial F}{\partial \xi_\mu}\Delta\xi_\mu^{(j)} \tag{3.32}$$

and from Eq. 3.21

$$\begin{aligned} c_m(k,s) &= \langle f_j f_{l+m}^*\rangle \\ &= \sum_{\mu\nu} \frac{\partial F}{\partial \xi_\mu}\frac{\partial F^*}{\partial \xi_\nu}\langle \Delta\xi_\mu^{(j)}\Delta\xi_\nu^{(j+m)}\rangle. \end{aligned} \tag{3.33}$$

Since the ensemble is assumed to be homogeneous, the correlations $\langle \Delta\xi_\mu^{(j)} \Delta\xi_\nu^{(j+m)} \rangle$ are independent of j, and will be denoted by $G_{\mu\nu}(m)$, i.e.,

$$G_{\mu\nu}(m) = \langle \Delta\xi_\mu^{(j)} \Delta\xi_\nu^{(j+m)} \rangle. \tag{3.34}$$

Moreover, they are independent of k and s, and assuming left-right invariance of the grating, they satisfy the symmetry relations

$$G_{\mu\nu}(m) = G_{\mu\nu}(-m) = G_{\nu\mu}(m). \tag{3.35}$$

From this symmetry it follows that $c_m(k,s)$ is real. Since $G_{\mu\nu}(m)$ is an even function of m, it may be represented as Fourier cosine series. In addition, from physical considerations the correlations must fall off with increasing $|m|$. For simplicity, assume that the correlations $G_{\mu\nu}(m)$ may be represented in the form

$$G_{\mu\nu}(m) = \sigma_{\mu\nu} e^{-\alpha_{\mu\nu}|m|} \cos(2\pi m \Omega_{\mu\nu}). \tag{3.36}$$

In terms of these correlations, the probability density for scattering from Eq. 3.20 may be expressed as

$$\frac{kd}{2\pi} \sum_{\mu\nu} \sigma_{\mu\nu} \frac{\partial F}{\partial \xi_\mu} \frac{\partial F^*}{\partial \xi_\nu} \left[\sum_{m=-\infty}^{\infty} e^{imksd} e^{-\alpha_{\mu\nu}|m|} \cos(2\pi m \Omega_{\mu\nu}) \right]. \tag{3.37}$$

In deriving this equation, the exponential fall off of the correlations have allowed the sum to extended to all m. The sum over m may be performed by writing the cosine in its complex representation and recognizing that the resulting sum is geometric. It is left as an exercise for the reader to show that

$$\begin{aligned} \sum_{m=-\infty}^{\infty} & e^{imksd} e^{-\alpha|m|} \cos(2\pi m \Omega) \\ &= \frac{1+e^{-\alpha}}{2} \left[\frac{1-e^{-\alpha}}{(1-e^{-\alpha})^2 + 2e^{-\alpha}(1-\cos(ksd+2\pi\Omega))} \right. \\ &\qquad \left. + \frac{1-e^{-\alpha}}{(1-e^{-\alpha})^2 + 2e^{-\alpha}(1-\cos(ksd-2\pi\Omega))} \right] \end{aligned} \tag{3.38}$$

The right hand side of this equation shows that the correlations will produce peaks whenever $\cos(ksd \pm 2\pi\Omega)$ is unity, i.e., at values of s when $ksd/2\pi = n \pm \Omega$. In other words, *the scattering will consist of peaks that are symmetrically located about the diffraction orders*, although the strength of the peaks will depend upon the exact form of $c_m(k,s)$. A quick glance at Figure 6.19 shows that the peaks immediately to the left and right of first order have this property. In addition, the data has a peak just to the right of third order and it appears to have a small peak symmetrically placed at the left of third order. It is harder to make the argument about second order because if there is a peak to the left of second order then it is suppressed.

The location of the peaks and their widths provide valuable information about the parameters Ω and α. In particular the location of the peaks give information about Ω, and their widths are governed by α. To see this, suppose that α and $\theta = ksd + 2\pi\Omega$ are small. Then the first term term on the right hand side of Eq. 3.38 may be approximated by

$$\frac{\alpha}{\alpha^2 + \theta^2}. \tag{3.39}$$

This function has a maximum at $\theta = 0$ and the half-width at half-maximum is α. Hence, the width of the scattering peak provides information about α, which in turn dictates the range of the correlation responsible for the peak. Armed with this knowledge one can make a rough estimate of Ω and α for the correlation associated with the peaks closest to the diffraction orders of Figure 6.19. We estimate Ω to be around 0.1 and α to be roughly $0.05 \times 2\pi \approx 0.3$. This implies that the correlations have a length of $1/\alpha$ or about 3 grating bars.

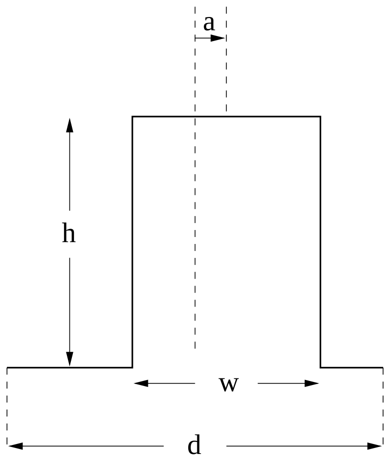

Figure 3.22: Figure showing the geometric parameters for a rectangular grating bar of width w and height h in a unit cell with period d. The displacement of the bar from the center of the unit cell is given by a.

3.3.5 Correlations in the Rectangular Model

In this section, we assume that the grating bar shapes may be represented by a simple rectangle with height h and width w. The center of the bar is assumed to offset a distance a from the center of the lattice node (see Figure 3.22).

The rectangular geometry readily permits the integral in Eq. 3.8 to computed with the result

$$F_j(k,s) = \frac{\sin(\frac{1}{2}ksd)}{\frac{1}{2}ksd} + e^{iksa_j}(e^{-kh_j\beta - ikh_j\delta} - 1)\frac{\sin(\frac{1}{2}ksw_j)}{\frac{1}{2}ksd}. \tag{3.40}$$

As in the previous section, we assume that the correlations are small so that Eq. 3.33 is valid. Expressing Eq. 3.33 in terms of h, w, and a, results in

$$\begin{aligned} c_m(k,s) =& d^2\left|\frac{\partial F}{\partial a}\right|^2 G_{aa}(m) + h^2\left|\frac{\partial F}{\partial h}\right|^2 G_{hh}(m) + d^2\left|\frac{\partial F}{\partial w}\right|^2 G_{ww}(m) \\ &+ 2hd\,\mathrm{Re}\left[\frac{\partial F}{\partial a}\frac{\partial F^*}{\partial h}\right] G_{ah}(m) + 2hd\,\mathrm{Re}\left[\frac{\partial F}{\partial w}\frac{\partial F^*}{\partial h}\right] G_{wh}(m) \\ &+ 2d^2\,\mathrm{Re}\left[\frac{\partial F}{\partial a}\frac{\partial F^*}{\partial w}\right] G_{aw}(m), \end{aligned} \tag{3.41}$$

where factors of d and h have been introduced to make the correlation functions $G_{\mu\nu}(m)$ unitless, e.g.,

$$\begin{aligned} G_{wh}(m) &= \langle \frac{\Delta w}{d}\frac{\Delta h}{h} \rangle \\ &= \sigma_{wh} e^{-\alpha_{wh}|m|} \cos(2\pi m \Omega_{wh}). \end{aligned} \tag{3.42}$$

The partial derivatives of the structure factor $F(k,s)$ are rather straightforward to carry out

h	$=$	0.64μm	w/d	$=$	0.84			
σ_{ww}	$=$	6.5×10^{-5}	α_{ww}	$=$	0.27	Ω_{ww}	$=$	0.092
σ_{hh}	$=$	5.0×10^{-5}	α_{hh}	$=$	0.60	Ω_{hh}	$=$	0.50
σ_{wh}	$=$	4.2×10^{-5}	α_{wh}	$=$	0.30	Ω_{wh}	$=$	0.91

Table 3.2: This table shows the best fit parameter values as deduced from fitting the scattering data at 1.384, 1.775, and 2.035 keV. Displacement variations were not considered. Figure 3.23 shows the resulting fit.

with the result:

$$
\begin{aligned}
\left|\frac{\partial F}{\partial a}\right|^2 &= \frac{4}{d^2}[1 - 2e^{-kh\beta}\cos(kh\delta) + e^{-2kh\beta}]\sin^2(\frac{1}{2}ksw) \\
\left|\frac{\partial F}{\partial w}\right|^2 &= \frac{1}{d^2}[1 - 2e^{-kh\beta}\cos(kh\delta) + e^{-2kh\beta}]\cos^2(\frac{1}{2}ksw) \\
\left|\frac{\partial F}{\partial h}\right|^2 &= k^2(\delta^2 + \beta^2)e^{-2kh\beta}\left[\frac{\sin(\frac{1}{2}ksw)}{\frac{1}{2}ksd}\right]^2 \\
\mathrm{Re}\left[\frac{\partial F}{\partial w}\frac{\partial F^*}{\partial h}\right] &= \frac{k}{d}e^{-kh\beta}\left[\beta\cos(kh\delta) + \delta\sin(kh\delta) - \beta e^{-kh\beta}\right]\frac{\sin(ksw)}{ksd} \\
\mathrm{Re}\left[\frac{\partial F}{\partial a}\frac{\partial F^*}{\partial h}\right] &= \frac{4k}{d}e^{-kh\beta}\left[-\beta\sin(kh\delta) + \delta\cos(kh\delta) - \delta e^{-kh\beta}\right]\frac{\sin^2(\frac{1}{2}ksw)}{ksd} \\
\mathrm{Re}\left[\frac{\partial F}{\partial a}\frac{\partial F^*}{\partial w}\right] &= 0,
\end{aligned}
\tag{3.43}
$$

This model contains 17 independent parameters that include the bar width w and height h as well as the 15 parameters that define the correlation functions $G_{\mu\nu}(m)$. A χ^2 minimization procedure based upon the Marquardt algorithm[7] was used in deducing the parameters. Since the scattering contains energy-dependent terms, a global fit to the scattering data at 1.384, 1.775, and 2.035 keV was performed. These particular data were used because we feel that they have the the least experimental uncertainties and would provide the best estimates for the parameters.

We first considered the case involving no correlations. This reduced the parameter space from 17 dimensions down to 5. Figure 3.21 shows the best fit of the rectangular model with no correlations to the data 1.775 keV. From the figure, one can immediately see that the model without correlations fails to reproduce any of the rich structure seen in the data. The lack of any prominent scattering features is a strong indication that the grating scatter must be the result of correlations.

Figure 3.23 shows the result of a simultaneous fit to the 1.384, 1.775, and 2.035 keV scattering data when correlations were included. The parameters deduced from the fit are presented in Table 3.2. Fluctuations involving the bar displacement a were not included in this fit, reducing the number of free parameters down to 11 (including them did not substantially improve the fit so we felt that it was better to restrict the model to 11 parameters).

We can immediately see that including correlations results in a dramatic improvement of the fit. Although not perfect, this model shows all the main features in the scattering data at these

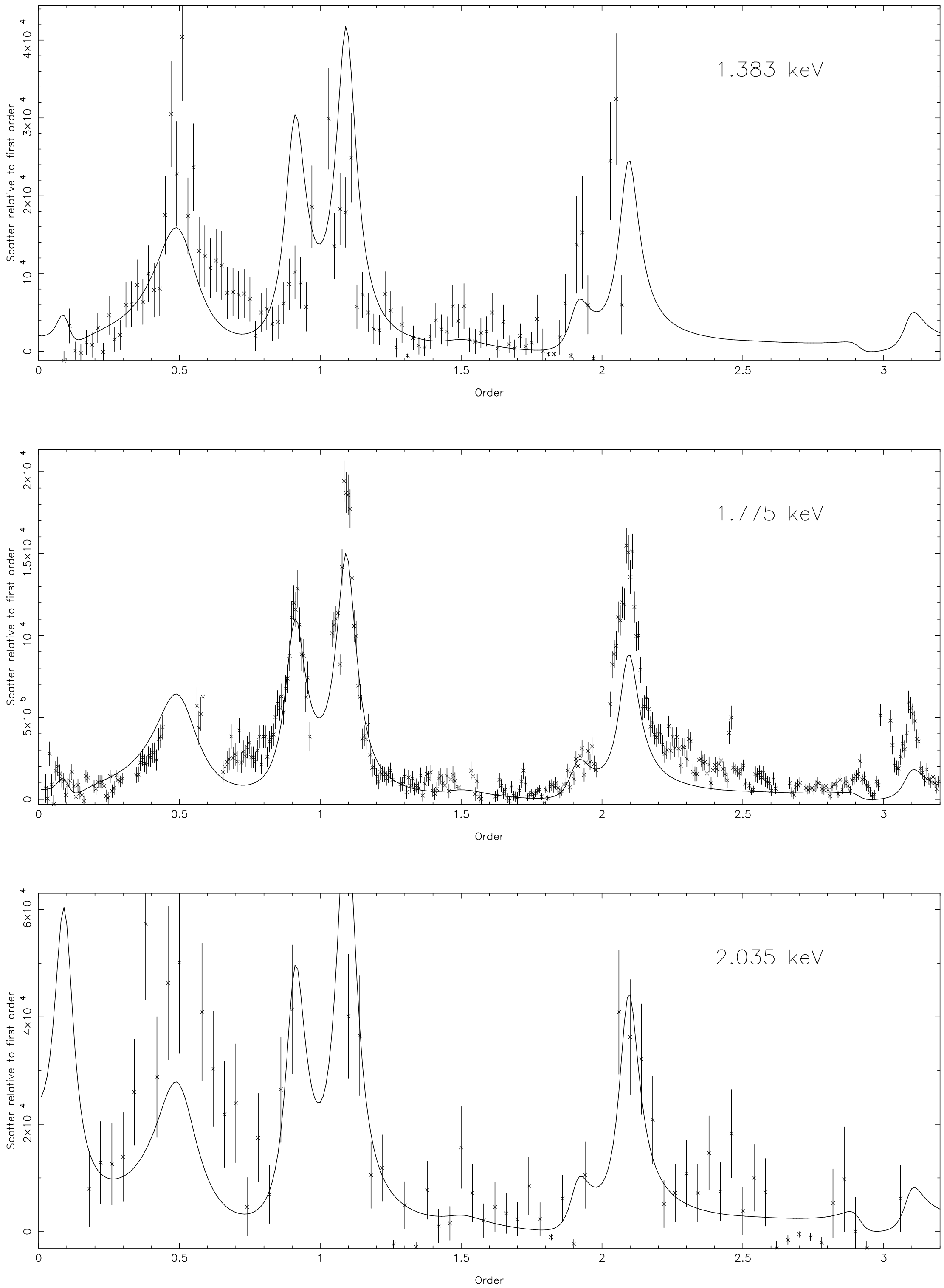

Figure 3.23: Results of a global fit to the 1.384, 1.775, and 2.035 keV scattering data. The model included width-width, height-height, and width-height correlations.

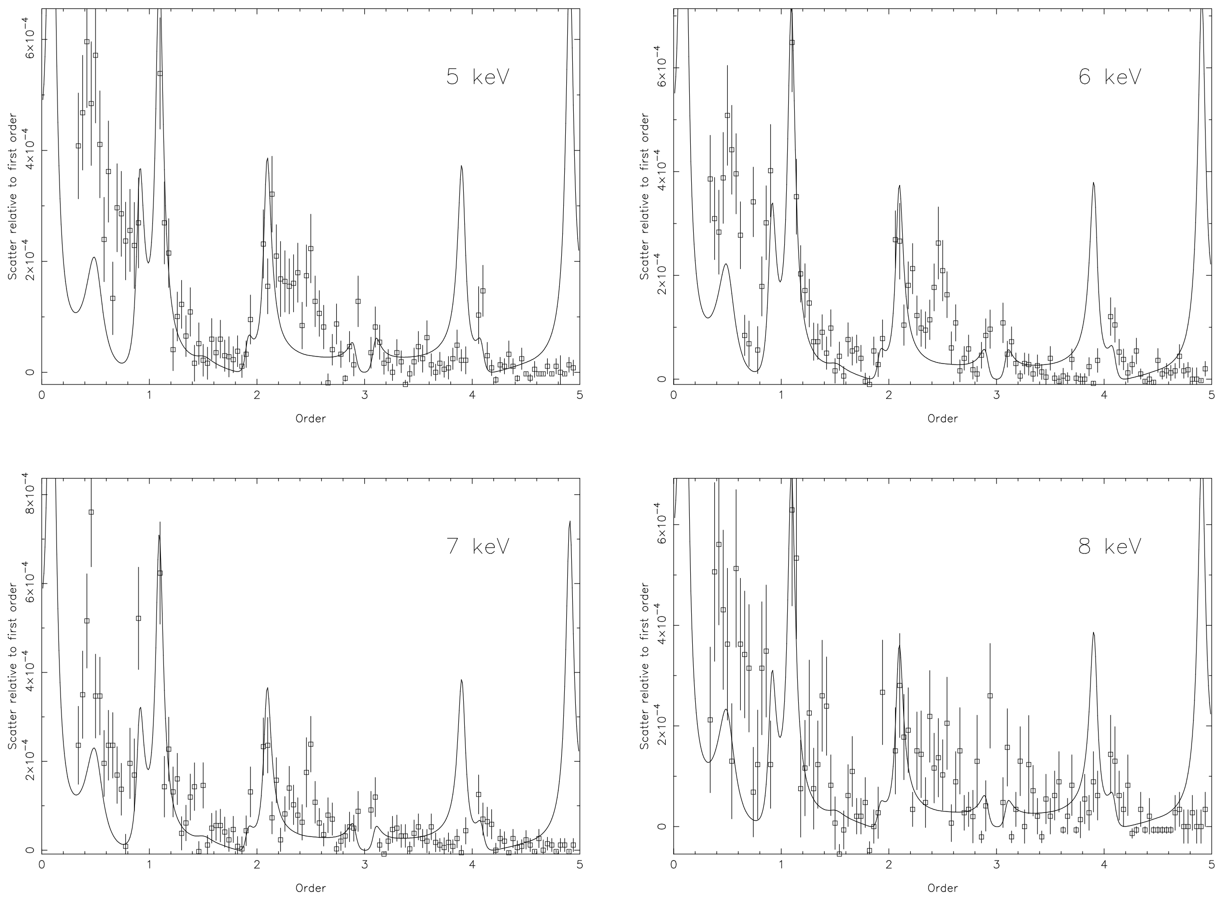

Figure 3.24: These figures show the predictions of the correlation model of Figure 3.23 evaluated at at 5, 6, 7, and 8 keV overlaid with the scattering data at these energies.

energies. This is especially true for our best data set, the data at 1.775 keV. The main areas of disagreement are near the half order locations, and at the second and third order scattering peaks where it underestimates the scattering. Also the average effective-rectangular bar width resulting from the fit is about 35 percent larger than the accepted average width: w/d is 0.84 compared to $w/d \approx 0.60$ based on detailed vertex-model fits[47] to the facet data[58]. Nevertheless, we feel that the fit is remarkable considering the simplicity and known shortcomings of the model.

Figure 3.24 shows the predictions of the model at higher energies ($5 - 8$ keV) overlaid with scattering data at those energies. The model is not too bad at predicting the scatter between the first and third orders in the high energy data, although it performs poorly when extrapolated past third order. This should not be too surprising since the data used to determine the model's parameters did not extend past third order.

3.3.6 Discussion

While the fit adequately reproduces many of the features observed in the data, the real physics lies in the form of the correlation functions deduced from the fit. A plot of the three correlation

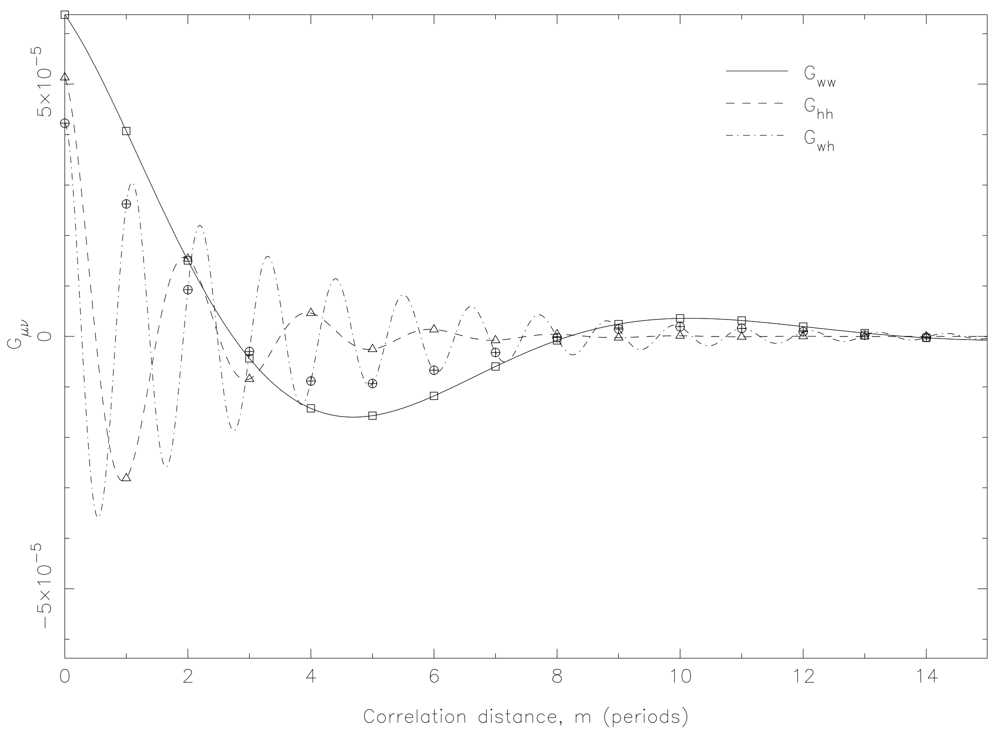

Figure 3.25: This figure shows a plot of the correlation functions parameterized in Eq. 3.36 using the parameters from Table 3.2.

functions $G_{ww}(m)$, $G_{hh}(m)$, and $G_{wh}(m)$ is shown in Figure 3.25. The dominate correlation is $G_{ww}(m)$, i.e., the width-width correlation. As can been seen from the figure, the shape of this correlation implies that the grating bar widths of the first and second nearest neighbor bars are positively correlated whereas the widths of the fourth and fifth nearest neighbors are anti-correlated. Physically, this correlation could arise by groups of two or three grating bars leaning in the same general direction. It is this correlation that appears to be responsible for the strong peaks closest to the diffraction orders.

The form of the height-height correlations, $G_{hh}(m)$, indicate that heights of nearest neighbors are anti-correlated. This has the effect of doubling the grating period and it is this correlation that contributes to the scattering near the half-orders. The simplest physical picture of this type of correlation is that of the left and right nearest neighbors leaning in the direction of the central bar.

One must not come to the conclusion that these physical pictures of the width-width and height-height correlations are mutually exclusive. Indeed there is nothing that prevents the gratings from having both types of disorder because each type may occur at disjoint parts of the grating. Thus the physical picture that emerges from these correlations is that the grating consists of localized groups of leaning bars and that the groups may be classified according to at least two varieties. The first type consists of several bars that lean in the same direction, possibly three or four together. The second type of fluctuation involves a group of three bars where the left and right bar leans on the central one. The final correlation, $G_{wh}(m)$, can be though of as the result of a combination of these two physical pictures.

If the explanation of the source of the correlations is correct, then the size of the correlations

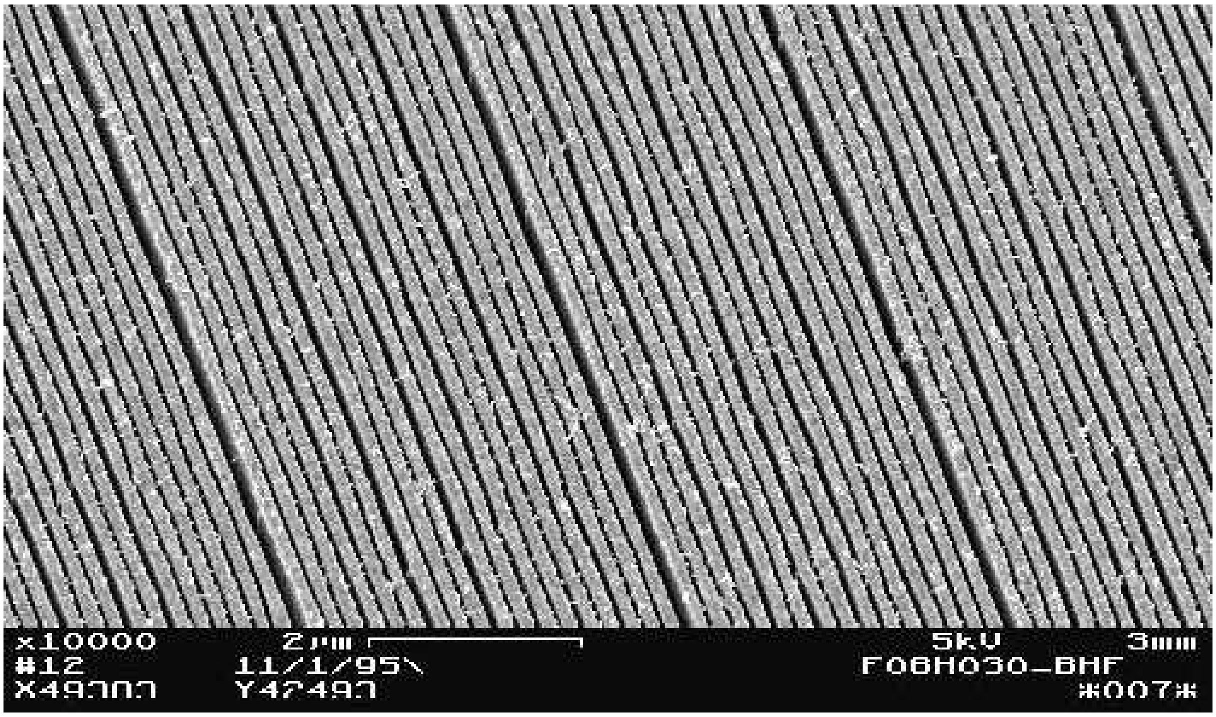

Figure 3.26: Electron micrograph of gold HEG bars on a monitor sample. The sample, F06H030b, is from flight fabrication lot 6; 6 of the 144 flight HEGs are from the same lot.

may be used to deduce the frequency of such fluctuations. For example, consider the width-width correlation, which is roughly 10^{-4} and implies that the fluctuation $\Delta w/d$ is 0.01 or about 1 percent of the period. This is consistent with 1 in 200 grating bars having a fluctuation in width by half a period, while the other 199 bars do not fluctuate at all.

Finally, if the scattering is due to the presence of leaning bars, then the absence of any detectable scattering by the MEG gratings is very easy to understand. The MEG gratings have a bar width of about 0.2 microns, and a bar height of about 0.36 microns. Hence, compared to the HEG gratings, which have a height to width ratio of about 5, the MEG gratings have a height to width ratio that is less than 2, and would be much less likely to lean.

3.3.7 Conclusion and Next Steps

Despite the apparent simplicity of both the rectangular model and the assumed form of the correlations, the resulting fits to the data are relatively good. The primary goal of this work was to demonstrate that the observed scatter could be the result of imperfections in the gratings and not to some other more exotic physical explanation. We are quite content that this goal has been achieved and we believe that the rectangular model has served us quite well in this regard.

Nevertheless, the fits are far from perfect and there are several discrepancies that should be accounted for by a more accurate and sophisticated model. Over 144 distinct grating facets contributed to the scatter and it is not inconceivable that a better fit could be achieved by using more than one set of bar parameters. This is perhaps the most trivial extension of the simple rectangular model used here. Also, we assumed that the deviations in the bar parameters from their ideal values were small enough that only first order deviations were important. Although the average fluctuation was found to be very small, any one bar parameter could deviate significantly from its mean, with the implication that higher order terms in the expansion could be significant.

Since the actual bars have path-length functions that are more trapezoidally shaped than rectangular, it makes more sense to consider a model involving trapezoidal bars. Such a model would also permit a more direct study of leaning bars— something that is not possible within the confines of the rectangular model. Finally, there are other components of the gratings that have been totally ignored in this work, and the fluctuations in these quantities could contribute to scatter. A more complete treatment would also include these fluctuations, e.g., fluctuations in the plating base as well as in the thickness of the polyimide film.

3.4 Efficiency Software

The efficiency modeling software used to study synchrotron data, analyze laboratory data, and create the HETG efficiency values is the multi-vertex efficiency code written by John E. Davis. Key routines are written in "C" and compiled into the executable "eff". This executable can be controlled through scripts written in S-Lang, *e.g.*, `multi.sl`.

The `multi.sl` program takes a file with one or more multi-vertex-grating-parameter-sets and calculates the average efficiency at a set of energies and range of orders. Specifically, the files required for efficiency calculation are

- eff - executable containing efficiency intrinsic functions
- optical-constants.tbl - data file of material X-ray properties
- energy.dat - an ASCII list of output energies desired
- multi.sl - the S-Lang ASCII program which directs the calculation
- multi_params.txt - the model parameters of the grating(s)

The calculation is executed by typing to unix:

```
unix_prompt% /[eff_path]/eff multi.sl
```

and an output efficiency file is created.